

Design and Implementation of a 3-Axis Biopsy Robot Powered, Imaged, and Controlled by MRI

Aaron Becker, Ouajdi Felfoul, Remy Kaldwy, and Pierre E. Dupont

Abstract—Actuators that are powered, imaged, and controlled by Magnetic Resonance (MR) scanners can inexpensively provide wireless control of MR-guided robots. Similar to traditional electric motors, the MR scanner acts as the stator and generates propulsive torques on actuator rotors containing one or more ferrous particles. This paper designs and implements a needle biopsy robot operated by three MRI actuators. This paper provides detail on designing, imaging, and controlling a multiple-DOF MRI actuator.

I. INTRODUCTION

THIS paper presents progress on a three-DOF needle biopsy robot wirelessly powered, imaged, and controlled by an unaltered clinical MR scanner. Robots can be powered, imaged, and controlled using Magnetic Resonance Imaging (MRI) scanners [1]–[4]. This paper implements the control techniques for simultaneous control of MRI actuators proposed in [5].

Any ferrous material placed inside the bore of an MR scanner becomes strongly magnetized. The three orthogonal gradient magnetic fields inside the MRI can exert forces on the ferrous material. Though these gradient fields are controllable, they are relatively weak: the maximum force produced by a 40mT gradient field on a fully magnetized steel particle is only 71% the force of gravity. These maximum gradients require large current that cause heating of the coils and therefore cannot be applied for long durations. On a Skyra 3T MR scanner, the maximum gradient that can be constantly applied is 23 mT, which is 41% of the force of gravity on the same particle.

The force produced by the gradient fields can be magnified through a gear train.

II. RELATED WORK

A. MRI-powered robotics

moving capsules [6]

controlling multiple capsules with MRI [1]

B. MRI-compatible Robots

C. Needle Biopsy Robots

Needle insertion requires xx N of force (porcupine study [7], Dupont needle insertion [8])

A. Becker, O. Felfoul, and P. E. Dupont are with the Department of Cardiovascular Surgery, Boston Children's Hospital and Harvard Medical School, Boston, MA, 02115 USA `first.name.lastname@childrens.harvard.edu`. R. Kaldwy is a high school senior at Boston University Academy, Boston, MA 02215 USA `Remy_Kaldwy@buacademy.org`. This work was supported by the National Science Foundation under IIS-1208509 and by the Wyss Institute for Biologically Inspired Engineering.

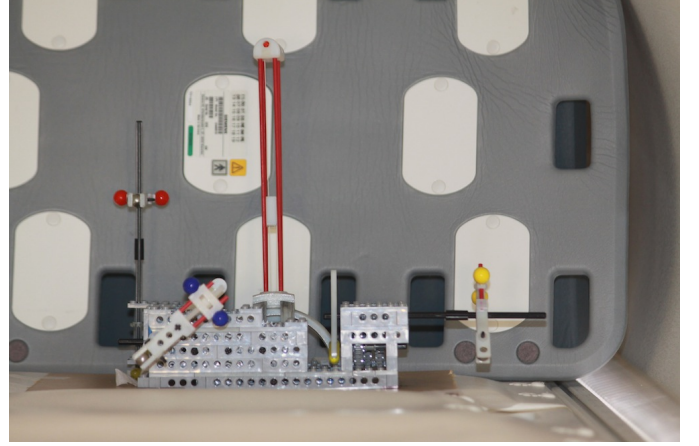


Fig. 1. The 3-DOF needle-biopsy robot described in this paper.

Previous work presented an MRI actuator that could drive a needle with up to 9.7 N of force [4].

III. THEORY

The theory of MRI multi-actuator control was introduced in [5], and based on work on work with single-axis MRI actuators [9], [10]. This section quickly reviews the theory, and then designs controllers for the biopsy robot with three orthogonal rotors.

A ferrous particle in the strong static field of an MRI becomes magnetized, and its magnetization magnitude asymptotically approaches the saturation magnetization M_s per unit volume of the material. The MRI gradient coils produce a magnetic field $\mathbf{B}_g(t)$. This field exerts on the ferrous particle the force

$$\mathbf{F}(t) = v (\mathbf{M}_s \cdot \nabla) \mathbf{B}_g(t). \quad (1)$$

Here v is the magnetic volume of the material. The magnetic field $\mathbf{B}_g(t)$ is designed to produce three independent gradients:

$$[F_x, F_y, F_z]^T(t) = v M_{sz} \left[\frac{\partial B_{gz}}{\partial x}, \frac{\partial B_{gz}}{\partial y}, \frac{\partial B_{gz}}{\partial z} \right]^T(t) \quad (2)$$

Here it has been reasonably assumed that $M_{sz} \gg M_{sx}, M_{sy}$. These gradients apply three independent forces on any ferromagnetic spheres inside the MRI. This paper investigates rotors that constrain the i th ferromagnetic sphere to rotate about an axis \mathbf{a}_i with a moment arm of length r_i , as shown in Fig. 2. The rotor's configuration is fully described by its angular position and velocity $[\theta_i, \dot{\theta}_i]^T$. The configuration space of all n rotors is $\mathbb{R}^{2 \times n}$, and the dynamic equations are

$$J_i \ddot{\theta}_i(t) = -b_i \dot{\theta}_i(t) - \tau_{fi} - \tau_{\ell i} + r_i \mathbf{F} \cdot \mathbf{p}_i(t) \quad (3)$$

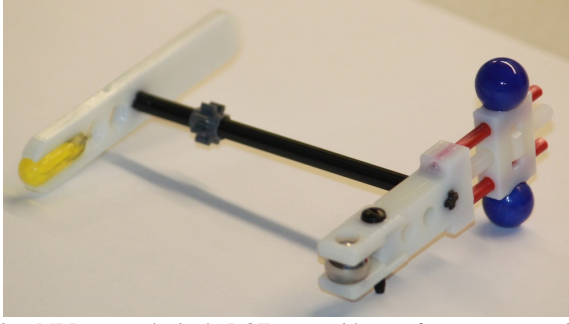


Fig. 2. MRI-powered, single-DOF rotor with gear for power transmission.

Here J_i is the moment of inertia, b_i the coefficient of viscous friction, τ_{f_i} the summation of all non-viscous friction terms seen by the input, and τ_{ℓ_i} the load torque. The rotor torque is the magnetic force projected to a vector tangent to the ferrous sphere's positive direction of motion, $r_i \mathbf{F} \cdot \mathbf{p}_i(t)$. Actuator torque is maximized when $\mathbf{F}(t) = g_M V M_{sz} \text{sgn}(\mathbf{p}_i(t))$, where g_M is the maximum gradient.

A. Open-loop control

B. Closed-loop control

C. Interleaving Sensing and Actuation

IV. DESIGN

The robot prototype is mostly 3D-printed, making the robot easily replicated at other institutions and hospitals with an MRI scanner. The 3D printed components were designed in SolidWorks, and are available at thingiverse.com¹. This illustrates how robot designs can be easily shared and working robots can be printed by third parties. This is similar to recent efforts to make printable robots, e.g. [11]. These efforts have created self-folding structures, but the motors and controllers are commercial devices that are currently manually added. In contrast, in this design the MRI scanner performs the difficult tasks of actuation and sensing, while the robot consists of a plastic 3D-printed structure and only requires adding a ferrous sphere for each actuator.

A. Motor Design

Contrasting architectures: linear vs rotary actuators. Needle driving: tendons vs timing belts vs friction rollers vs gear system. Needle replacement. Motor modularity. Required forces.

To study the preceding topics in the context of a practical example system, a three-axis biopsy robot powered by DC motors was considered [12]. Figure 1 shows a prototype that is powered and actuated by an MRI scanner. The system has a fixed base that is attached to the patient. Two actuators, θ_x and θ_y , control orthogonal axes of a nested spherical yoke. A carriage rides along the intersection of this yoke. Mounted on this carriage is a third actuator, θ_{needle} , that can insert a needle through a pivot point at the center of the base. The original design allows θ_x and θ_y to rotate between $[-\pi/6, \pi/6]$, and inserts θ_{needle} from $[0, 100]$ mm, resulting in a spherical quadrilateral workspace with volume

$(\theta_{needle})^3 \pi/9$. The base has diameter 100mm, and the nested yokes have radii 50mm.

The rotors attached to the spherical yokes are subject to a torque due to gravity, τ_{mass} , and a needle-depth dependent torque, τ_{needle} , as well as the frictional torques in (3).

$$\begin{aligned} \tau_{mass} &= mg\ell \sin(\theta_i) & [\text{Nmm}] \\ \tau_{needle} &= \theta_{needle} \frac{60}{100} & [\text{Nmm}] \end{aligned} \quad (4)$$

The lumped mass g of the carriage and needle actuator is 0.1kg and the yoke radius $\ell=50$ mm [12]. The frictional losses in the gear train are represented by $\eta_e \in [0, 1]$, a dimensionless parameter for motor efficiency.

The two yoke actuators require 100Nmm of torque and the needle actuator requires 50Nmm of torque. Assuming a conservative $\eta_e = 0.5$, with a gear reduction ratio G , the motor torque is

$$\tau_{motor} = \eta_r \eta_e G r_i \frac{4}{3} \pi r_{sphere}^3 M_{sz} g_M. \quad (5)$$

Here η_r is the average torque per rotor for $n = 3$ rotors, which was evaluated as ≈ 0.81 in [5]. Using a rotor radius of $r_i=20$ mm and a sphere radius $r_{sphere}=6$ mm, the yoke actuators require a gear reduction of $G_{xy}=250$, and the needle actuator requires $G_n=125$.

The ferrous spheres must be separated to minimize dipole-dipole forces, as will be described in Section IV-B. According to (9), to limit dipole-dipole forces to less than 10% of maximum gradient forces with 6mm radius ferrous spheres requires at least 116mm spacing.

B. Optimizing Spacing

There are several concerns when placing MRI actuators near each other: magnetic attraction between ferrous particles, linearly separable MRI fiducials, and minimizing the influence of ball-bearings on other actuator's fiducials.

a) *Fiducial offset*: The MRI fiducials must be accurately placed in the magnetic field generated by the ferrous ball bearing. The magnetic field is given by (7), with $\mathbf{m}_1 = [0, 0, 4/3\pi r_s^3 M_{sat}]^\top$. The fiducials should be placed where the magnetic field equals the ratio of the RF frequency offset f_{offset} , and the gyromagnetic ratio $\gamma = 42.48\text{MHz}$.

$$\begin{aligned} \mathbf{B}_{r1}(x, z) &= \frac{f}{\gamma} \\ d_{xy} &= \sqrt[3]{\frac{M_{sat} r_s^3 \mu_0 \gamma}{3 f_{offset}}} \\ d_z &= \sqrt[3]{2 \frac{M_{sat} r_s^3 \mu_0 \gamma}{3 f_{offset}}} \end{aligned} \quad (6)$$

For $r = 2.5$ mm alloy steel spheres, $d_{xy} \approx 0.047$ mm and $d_z \approx 0.060$ mm. $d_z = \sqrt[3]{2} d_{xy}$, and scale linearly with the ferrous sphere radius. The z axis actuator can only be imaged using positive frequency RF signals, and the x and y actuators must be imaged using negative RF signals, as shown in Fig. 3.

¹www.thingiverse.com/thing:449517

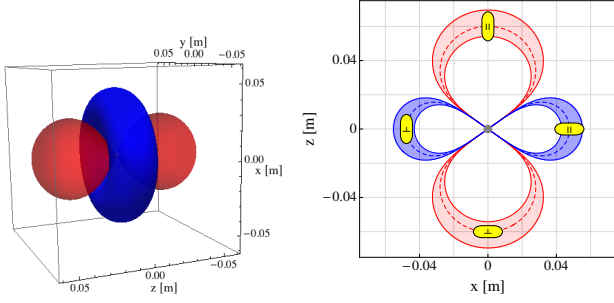


Fig. 3. To be imaged, MR fiducials (yellow) must be accurately placed in the magnetic field generated by the ferrous ball-bearing. Positive RF frequencies illuminate fiducial markers along the z axis (red) and negative RF frequencies illuminate fiducials in the xy plane (blue). These fiducial markers are optimally placed perpendicular to the rotor axis (\perp), not parallel (\parallel), because this places more fiducial liquid at the center RF frequency (dashed line).

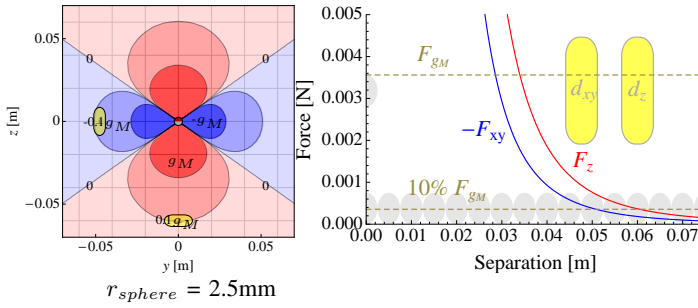


Fig. 4. One ferrous sphere in a 3T magnetic field exerts a force \mathbf{F} on an identical sphere. The contour lines show $\mathbf{F} \cdot \mathbf{n}_{12}$, the force component radially outward from the sphere at (0,0) compared to the maximum force provided by the gradient coils g_M . This force is attractive (red) along the z -axis and repulsive (blue) perpendicular to z . The magnetic field is symmetric about the z -axis. If two spheres move within the dark red region, they cannot be separated using the gradient field.

b) Ferrous-Ferrous spacing: Each rotor contains a ferrous ball-bearing, which will attract and repulse each other. These bearings must be placed far enough apart such that the forces exerted are negligible compared to the magnetic gradient.

Any ferrous material placed in the magnetic field of an MR scanner becomes a strong magnetic dipole. With multiple MR-powered motors, these dipoles exert forces on each other. Dipole forces overpower MRI gradient forces if rotors are closer than a threshold distance.

The magnetic field at position \mathbf{r}_2 generated by a spherical magnet at position \mathbf{r}_1 with magnetization \mathbf{m}_1 is [13]

$$\mathbf{B}_{\mathbf{r}_1}(\mathbf{r}_2) = \frac{\mu_0}{4\pi} \frac{3\mathbf{n}_{12}(\mathbf{n}_{12} \cdot \mathbf{m}_1) - \mathbf{m}_1}{|\mathbf{r}_2 - \mathbf{r}_1|^3}, \quad (7)$$

with $\mathbf{n}_{12} = (\mathbf{r}_2 - \mathbf{r}_1)/|\mathbf{r}_2 - \mathbf{r}_1|$. This is the magnetic field of a dipole. The force applied to a dipole at \mathbf{r}_1 with magnetic moment \mathbf{m}_1 by another dipole at \mathbf{r}_2 with magnetic moment \mathbf{m}_2 is approximated by

$$\mathbf{F}_{12} \approx \frac{3\mu_0}{4\pi} \frac{1}{|\mathbf{r}_2 - \mathbf{r}_1|^4} \left[5\mathbf{n}_{12} \left((\mathbf{m}_1 \cdot \mathbf{n}_{12}) (\mathbf{m}_2 \cdot \mathbf{n}_{12}) \right) - \mathbf{n}_{12} (\mathbf{m}_2 \cdot \mathbf{m}_1) - \mathbf{m}_1 (\mathbf{m}_2 \cdot \mathbf{n}_{12}) - \mathbf{m}_2 (\mathbf{m}_1 \cdot \mathbf{n}_{12}) \right].$$

Figure 4 shows contour plots for the magnetic force exerted

by two identical spheres on each other. The contour lines are drawn at $\mathbf{F}_{12} \cdot \mathbf{n}_{12} = g_M \cdot \{-1, -\frac{1}{10}, 0, \frac{1}{10}, 1\}$. The maximum force is along the z -axis

$$F_{\text{attraction}} = -\frac{8M_s^2\mu_0\pi r_1^3 r_2^3}{3d^4}, \quad (8)$$

where d is the distance separating two sphere of radius r_1 and r_2 , each with magnetic saturation M_s . For steel, $M_s = 1.36 \times 10^6$. The vacuum permeability μ_0 is, by definition, $4\pi \times 10^{-7} \text{ V} \cdot \text{s}/(\text{A} \cdot \text{m})$.

The critical distance when the attractive force becomes greater than the maximum gradient force is $\sqrt[4]{\frac{2M_s\mu_0 r_{\text{sphere}}^3}{g_M}}$. This interaction decays quickly and at distance $\approx 5.4r_{\text{sphere}}^{3/4}$ is 10% of the maximum gradient. The required distance, d , to ensure dipole-dipole forces are less than some percentage of the maximum gradient is given by

$$d \geq \sqrt[4]{\frac{2 \frac{100}{\text{percentage}} M_s \mu_0 r_{\text{sphere}}^3}{g_M}}. \quad (9)$$

c) Fiducial-Ferrous spacing: Moreover, fiducials must be separated from other ferrous ball-bearings. The magnetic field from ball bearings is additive, so ferrous ball-bearings must be spaced to avoid influencing non-associated MRI fiducials.

As shown in Fig. 5, if other ferrous particles are too close a fiducial may no longer be illuminated. (7), The ideal spacing between fiducial and ferrous particle is given by 6, and is defined as the distance where the magnetic field value equals the RF frequency offset. The MRI fiducials used have a radius of $r_{\text{fiducial}} = 3.5\text{mm}$. If the influence of another ferrous particle moves the magnetic field more than r_{fid} , the fiducial will be insufficiently illuminated. The minimum separation is found by solving for $d_{xy\text{Min}}$ and $d_{z\text{Min}}$:

$$\begin{aligned} \mathbf{B}_{(0,0)}(d_{xy} + r_{\text{fid}}, 0) + \mathbf{B}_{(d_{xy\text{Min}}, 0)}(d_{xy} + r_{\text{fid}}, 0) &= \frac{f_{\text{offset}}}{\gamma} \\ \mathbf{B}_{(0,0)}(0, d_z + r_{\text{fid}}) + \mathbf{B}_{(0, d_{z\text{Min}})}(0, d_z + r_{\text{fid}}) &= \frac{f_{\text{offset}}}{\gamma} \end{aligned} \quad (10)$$

For $r_s = 2.5\text{mm}$, $d_{xy\text{Min}} \approx 13\text{mm}$ and $d_{z\text{Min}} \approx 17\text{mm}$. A diamond shaped polygonal region with vertices at $(\pm d_{xy\text{Min}}, 0), (0, \pm d_{z\text{Min}})$ conservatively bounds the unsafe region, as shown in Fig. 5.

d) Fiducial-Fiducial spacing: The actuator axis and fiducials must be spaced such that their projections onto the x , y , and z axis are linearly separable. The fiducial projections are given in Table I using the trigonometric shorthand $\cos(\theta) = c_\theta$, $\sin(\theta) = s_\theta$. The z -axis rotors are imaged separately using a positive frequency, leaving three constraints:

$$\begin{aligned} x_x &\not\in x_y + d_{xy} \pm r \\ y_x &\not\in y_y - d_{xy} \pm r \\ z_x &\not\in z_y \pm 2r \end{aligned} \quad (11)$$

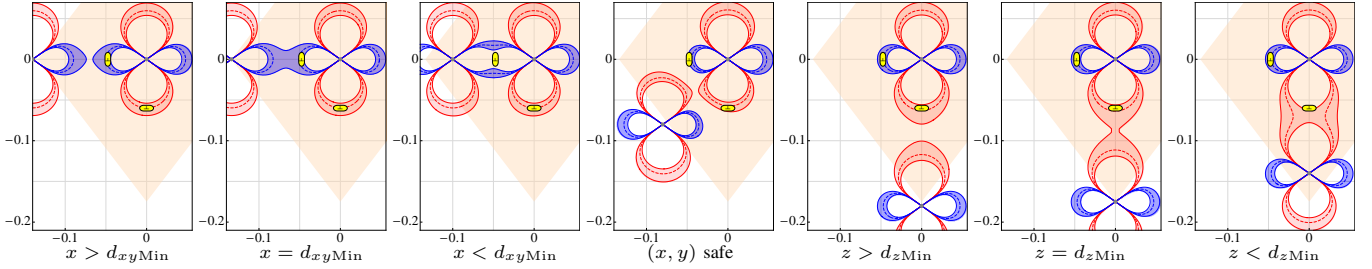


Fig. 5. The magnetic field due to ferrous particles is additive. The MRI fiducials are placed either d_x or d_{xy} distance from their corresponding ferrous particle to be illuminated by a certain RF frequency (dashed line). If other ferrous particles are too close, the fiducial will no longer be illuminated. The orange polygon conservatively defines this unsafe region.

axis	sphere center	projection		
		x	y	z
x	$[x_x, y_x, z_x]$	$x_x - d_{xy}$	$y_x + rc\theta_x$	$z_x + rs\theta_x$
y	$[x_y, y_y, z_y]$	$x_y + rc\theta_y$	$y_y - d_{xy}$	$z_y + rs\theta_y$
z	$[x_z, y_z, z_z]$	$x_z + rc\theta_z$	$y_z + rs\theta_z$	$z_z - d_z$

TABLE I

PROJECTIONS OF FIDUCIAL POSITION ONTO x, y , AND z AXES.

C. Material Selection

With the notable exception of the ferrous sphere made of E52100 Alloy Steel, the biopsy robot must be constructed of non-ferrous material. To avoid both burn dangers and damping forces due to eddy currents, materials must be non-conductive.

The robot is constructed of Vero White on an Alaris30 Objet printer braided suture cord for the tendon system, electrical grade fiberglass (GP03, www.mcmaster.com/2591K11) for long structural members

V. EXPERIMENTS

A series of experiments were conducted to quantify the power, efficiency, and speed of the actuator. The actuators were tested both individually and as a group.

A. Open-Loop

e) *Single-actuator actuation*: This experiment used an open-loop sinusoid rotating at XX Hz for XX seconds. The rotor completed XX spins, turning the

f) *Independent actuation*: report motor efficiency

g) *Maximum speed actuation*:

B. Closed-Loop

h) *Single-actuator actuation*:

i) *Independent actuation*: report motor efficiency

j) *Maximum speed actuation*:

C. Accuracy Test

D. Needle Imaging

A 22-gauge Chiba Biopsy Needle² was used and under MR control was inserted into a 50mm diameter lime. A 22-gauge needle has a diameter of 0.72 mm. A T1 weighted sequence T1-turbo spin echo with TR 1200 ms and TE 9.5ms transversal view. Slice thickness of 2 mm. INSERT IMAGE OF LIME

²DCHN-22-20.0-U

VI. CONCLUSIONS

A prototype

REFERENCES

- [1] P. Vartholomeos, M. Akhavan-Sharif, and P. E. Dupont, "Motion planning for multiple millimeter-scale magnetic capsules in a fluid environment," in *IEEE Int. Conf. Rob. Aut.*, May 2012, pp. 1927–1932.
- [2] P. Vartholomeos, C. Bergeles, L. Qin, and P. E. Dupont, "An MRI-powered and controlled actuator technology for tetherless robotic interventions," *Int. J. Rob. Res.*, vol. 32, no. 13, pp. 1536–1552, 2013.
- [3] A. Chanu, O. Felfoul, G. Beaudoin, and S. Martel, "Adapting the clinical MRI software environment for real-time navigation of an endovascular untethered ferromagnetic bead for future endovascular interventions," *Magn Reson Med*, vol. 59, no. 6, pp. 1287–1297, Jun. 2008.
- [4] O. Felfoul, A. Becker, C. Bergeles, and P. E. Dupont, "Achieving commutation control of an mri-powered robot actuator," *IEEE Trans. on Robotics*, vol. under review, 2014.
- [5] A. Becker, O. Felfoul, and P. E. Dupont, "Simultaneously powering and controlling many actuators with a clinical mri scanner," in *IEEE/RJS International Conference on Intelligent Robots and Systems (IROS)*, 2014, pp. 2017–2023.
- [6] S. Martel, J.-B. Mathieu, O. Felfoul, A. Chanu, E. Aboussouan, S. Tamaz, P. Poupponneau, L. Yahia, G. Beaudoin, G. Soulez, and M. Mankiewicz, "Automatic navigation of an untethered device in the artery of a living animal using a conventional clinical magnetic resonance imaging system," *Applied Physics Letters*, vol. 90, no. 11, pp. 114 105–114 105–3, Mar 2007.
- [7] W. K. Cho, J. A. Ankrum, D. Guo, S. A. Chester, S. Y. Yang, A. Kashyap, G. A. Campbell, R. J. Wood, R. K. Rijal, R. Karnik, R. Langer, and J. M. Karp, "Microstructured barbs on the north american porcupine quill enable easy tissue penetration and difficult removal," *Proceedings of the National Academy of Sciences*, vol. 109, no. 52, pp. 21 289–21 294, 2012. [Online]. Available: <http://www.pnas.org/content/109/52/21289.abstract>
- [8] M. Mahvash and P. Dupont, "Mechanics of dynamic needle insertion into a biological material," *Biomedical Engineering, IEEE Transactions on*, vol. 57, no. 4, pp. 934–943, April 2010.
- [9] C. Bergeles, P. Vartholomeos, L. Qin, and P. E. Dupont, "Closed-loop commutation control of an MRI-powered robot actuator," in *IEEE International Conference on Robotics and Automation*, May 2013, pp. 690–695.
- [10] P. Vartholomeos, L. Qin, and P. E. Dupont, "MRI-powered actuators for robotic interventions," in *IEEE Int. Rob. and Sys.*, 2011, pp. 4508–4515.
- [11] S. Felton, M. Tolley, E. Demaine, D. Rus, and R. Wood, "A method for building self-folding machines," *Science*, vol. 345, no. 6197, pp. 644–646, 2014. [Online]. Available: <http://www.sciencemag.org/content/345/6197/644.abstract>
- [12] C. J. Walsh, "Image-guided robots for dot-matrix tumor ablation," Ph.D. dissertation, Massachusetts Institute of Technology, 2010.
- [13] R. Schill, "General relation for the vector magnetic field of a circular current loop: a closer look," *Magnetics, IEEE Transactions on*, vol. 39, no. 2, pp. 961–967, Mar 2003.